IEEE Open Journal of the
Industrial Electronics Society

Received 28 February 2021; revised 28 March 2021; accepted 6 April 2021. Date of publication 14 April 2021;
date of current version 20 May 2021. The review of this article was arranged by Associate Editor Giampaolo Buticchi.

Digital Object Identifier 10.1109/OJIES.2021.3073142

Operation of Meshed Hybrid Microgrid During Adverse Grid Conditions With Storage Integrated Smart Transformer

HRISHIKESAN V M (Student Member, IEEE), AND CHANDAN KUMAR (Senior Member, IEEE)

Indian Institute of Technology Guwahati, Guwahati, Assam 781039, India

CORRESPONDING AUTHOR: Chandan Kumar (e-mail: chandank@iitg.ac.in)

This work was supported in part by "Visvesvaraya Ph.D. Scheme, MeitY, Govt. of India MEITY-PHD-1228," and in part by Science and Engineering Research Board (SERB), Department of Science and Technology, India, under Grant ECR/2017/001564.

ABSTRACT Microgrid faces various challenges such as reverse power flow, peak power demand, voltage limit violations, etc., due to significant installations of renewable energy sources (RESs) and electric vehicles (EVs). For continuous and effective operation of such a system, enhanced and complex control methodologies are needed. Smart transformer (ST) has emerged as a promising solution for overcoming such challenging issues. This paper proposes the operation of battery energy storage system (BESS) integrated ST in a meshed hybrid microgrid. Instead of connecting through ac interconnections with normally open (NO) circuit breakers (CBs), the same line is connected through the medium voltage (MV) dc links of ST. This introduces several paths for controlled power flow in the system. As compared to ac interconnections, this configuration improves the performance of the overall system during various adverse operating conditions such as reverse power flow, peak power demand, and voltage sag. Moreover, the MVDC line voltage is controlled by one ST, resulting in reduced control complexity of other power converters. Detailed simulation and experimental results are provided to show the merits of the proposed system.

INDEX TERMS Microgrid, photovoltaic (PV) integration, Smart transformer (ST).

I. INTRODUCTION

Renewable energy sources (RESs) such as photovoltaic (PV), wind, etc. are emerging as a sustainable solution for growing energy needs. However, the geographical distribution of these sources results in more distributed energy production in the grid [1]. The local consumption of energy reduces the line active power losses, and the co-existence of generation and loads constitutes the creation of ac microgrids in the power system [2]. The peak power production from PV sources leads to high reverse power flow in the microgrid during low-load hours, and voltage magnitude rise can cause irreversible damage to the connected equipments [3]. The peak power demand is another issue that requires immediate attention which may force the system operators to impose load shedding measures during peak demand hours [4]. Voltage sags are also a frequently occurring disturbance in the microgrid that affect the reliability of power supply.

Conventionally, the voltage rise due to reverse power flow is handled by solutions such as on-load tap changers (OLTCs) [5], and active power control of PV inverters [6]. The peak demand management is handled with battery energy storage system (BESS) [4], and voltage sags are mitigated using different active and reactive power control methods [7]. The OLTC based voltage control solutions are having a limited range of operation, whereas active power control from PV inverters reduces the overall energy extraction. Effectiveness of voltage sag mitigation techniques largely depends on the grid impedance and available active/reactive power capacity. The ac interconnections with normally open (NO) circuit breakers (CBs) are conventionally used for the microgrid interconnections, however, the system has limited power control features. In this scenario, the medium voltage (MV) dc interconnection to the ac microgrids provide advantages such as flexible active power transfer capability, independent active

and reactive power management, and improved stability [8], [9]. The power electronic converters that are used to integrate AC and DC systems can flexibly transfer active power in both directions. Therefore, the MVDC systems are used to connect the renewable-rich distribution grid with the main grid. The grids with more number of RESs lacks the inertia due the less number of synchronous generators. Therefore, sudden load and generation fluctuations can introduce frequency deviations in the grid and that can lead to instability. In these scenarios, the MVDC/HVDC interconnection can serve as an energy source and the interconnecting power electronic converter can be controlled as a virtual synchronous generator [10], [11]. Moreover, the MVDC systems are used for the horizontal coupling of substations and formation of meshed grids [12]. For the formation of hybrid ac/dc grids, various methods to convert the existing ac distribution lines to dc are detailed in [13].

The power electronic-based smart transformer (ST) has emerged as an effective choice for interfacing ac and dc systems [14]. A three-stage ST consists of dc links at MV and low voltage (LV) levels which are useful for establishing dc distribution systems [15], [16]. In addition, RES, BESS and electric vehicle (EV) charging station integrations are possible with the dc links [17]. Even though the conventional power transformers (CPTs) are more reliable in comparison with ST, continuous research is being conducted to improve the reliability of ST. Various solutions for improving the reliability of ST are proposed such as, the improved SiC device based MV technologies [18], modular power converter structure [19], power routing based on thermal loading [20], etc. Moreover, various other solutions proposed for improving power converter reliability can also be incorporated with ST [21], [22]. All these research methods are expected to improve the reliability of ST in the future applications.

The STs potential has been identified in providing several features such as the formation of an LVDC meshed hybrid distribution grid [23], hosting capacity enhancement [24], state of charge (SoC) management of BESS [25], MVDC interconnection [26], [27], frequency regulation [28], etc. The MVAC grid voltage support during voltage sag is investigated with ST in different scenarios [29]–[31]. The reactive power capability of ST MV converter is utilized to mitigate the voltage sag in [29], [30]. In addition, the active power is also used to support the voltage in MVAC grid [31]. The reverse power flow from LVAC to MVAC distribution grid is controlled by ST [32]. This method utilizes the ST LV converter control to curtail the active power from the RES during reverse power flow conditions.

Connecting LVAC lines between two grids is an option in ST-CPT based distribution system [33]. Similarly, the interconnection of MVDC links of STs is an option to provide more flexible operation for a microgrid during adverse MVAC grid conditions. This paper explores features of an MVDC interconnected, ST enabled, meshed hybrid microgrid configuration with BESS integration. The operation of the system is analyzed during peak PV generation, peak load demand

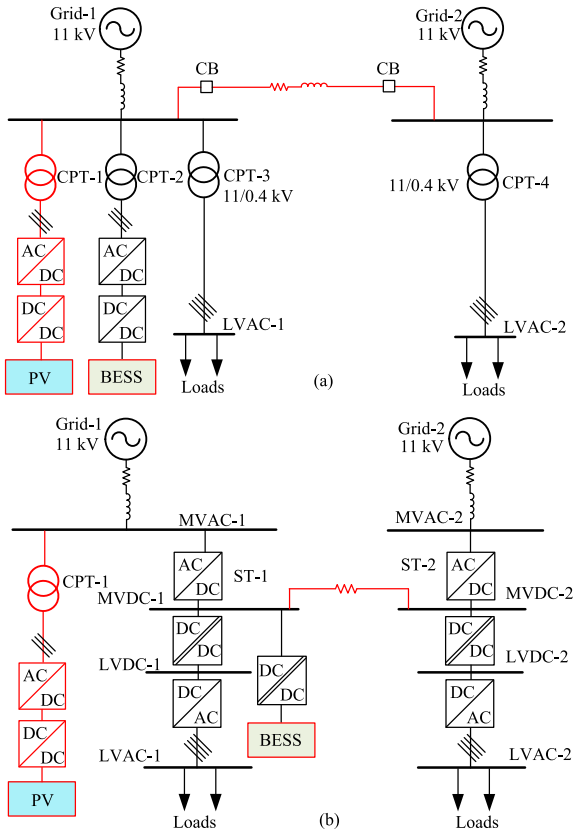

FIGURE 1. Single-line diagram of the system. (a) Conventional ac microgrid [12]. (b) ST based meshed hybrid system.

from MVAC grid and MVAC voltage sag in the microgrid. The main contributions of this paper are summarized as follows:

- The active power support during peak load hours is analyzed using BESS and MVDC interconnection.
- The capability of the system to control the reverse power flow is analyzed during peak PV generation period.
- The operation is analyzed during MVAC voltage sag condition to explore the potential of the system in providing reliable power supply to the LVAC loads.
- All the operating modes are verified with simulation and experimental results.

The organization of this paper is as follows: system configuration is discussed in Section II. Modes of operation are explained in Section III. Control of ST and BESS power converters is given in Section IV. Simulation and experimental analysis are provided in Section V, and Section VI, respectively. Major conclusions are reported in Section VII.

II. SYSTEM CONFIGURATION

Fig. 1(a) shows the conventional microgrid configuration connected to a second grid through ac distribution lines with NO CBs derived from [12]. The PV-based distributed generation (DG) source is connected to the MVAC bus of grid-1 through dc/dc, dc/ac converters and CPT. The BESS is connected to the grid-1 through dc/dc, dc/ac converters and CPT. The loads are connected to the LVAC-1 bus through the 11/0.4 kV CPT.

TABLE 1 System Parameters

System quantities	Values
MVAC voltage	11 kV (L-L)
LVAC voltage	0.4 kV (L-L)
LVAC-1, LVAC-2 loads	0.45 MW, 0.15 MVAr
ST MV converters	0.55 MVA
ST dc-dc converters	0.45 MW
ST LV converters	0.475 MVA
PV converters	0.45 MW
BESS converters	0.2 MW
BESS capacity	0.2 MWh

In grid-2 MVAC bus, loads are connected through 11/0.4 kV CPT.

The system configuration considered for analysis in this paper is shown in Fig. 1(b). In the ST based configuration, ST-1 and ST-2 replaces the CPT-2, CPT-3 and CPT-4 as shown in Fig. 1(b). The ST MVDC link has the capability to integrate PV. However, normally the MVAC grid contains multiple number of PV sources and restructuring one PV source to the MVDC link will not help in controlling the issue of reverse power flow. Therefore, the PV source connection in the ST based configuration remains same as shown in Fig. 1(a). The existing interconnecting ac distribution line is converted to an MVDC system, and connected between MVDC-1 and MVDC-2 [13]. BESS is connected to MVDC-1 through an isolated dual active bridge (DAB) converter [34]. The DAB is used in the BESS application because, it needs to be connected between an MVDC level and a battery terminal voltage level. This variation in the range of voltage is difficult to achieve without a transformer isolation, and DAB is considered as a better solution in this scenario. The DAB converter provides advantages such as good conversion efficiency, easy parallel and series connections for expanding the operation to higher voltage and current levels, etc. The STs use a three-stage configuration and the MV converter is a three-level ac-dc converter [15]. The dc-dc converter is a DAB converter with a high frequency transformer between MVDC and LVDC links [35]. The dc-ac converter uses a three-phase, two-level, dc-ac converter [15]. The ST-1 and ST-2 form LVAC buses and loads in grid-1 and grid-2 are connected to LVAC-1 and LVAC-2 buses, respectively. The parameters are shown in Table 1. The rating of ST converters are given in Table 1. A non-uniform sizing is adapted to the ST converters based on the requirement of distribution grid [14]. The ST LV converter rating is selected to supply the maximum active and reactive power load on LVAC bus. The ST DC-DC converter is sized to transfer the maximum active power load on the LVAC bus. The ST MV converter rating is selected to exchange the maximum active power load on ST LV converter. In addition, it is designed to transfer active power to the BESS or grid-2 at the LVAC full load condition.

III. MODES OF OPERATION

This paper considers four modes of operation, and they are named as mode-1, mode-2, mode-3, and mode-4. Also, transition of operation from one mode to another is discussed in this section. The power flow diagram for various modes of operation is shown in Fig. 2. The active power flow directions are also marked in all the diagrams. P_{mv1}, P_{mv2} and P_{bess} are the power flow through ST-1 MV, ST-2 MV and BESS converters respectively. P_t is the active power transfer through the MVDC line. Fig. 3 shows a flow-chart of the operating modes.

A. MODE-1: NORMAL OPERATION

The mode-1 power flow diagram is shown in Fig. 2(a). In the normal operation, the ST-1 and ST-2 supplies the LVAC-1 and LVAC-2 loads, respectively. In addition, the BESS charging is carried out through the ST-1 MV converter to maintain appropriate SoC. The active power references for MV converters of ST-1 (P^*_{mv1}) and ST-2 (P^*_{mv2}) are given by,

$$\begin{aligned} P^*_{mv1} &= P_{lv1-load} + P^*_{bess} \\ P^*_{mv2} &= P_{lv2-load} \end{aligned} \tag{1}$$

where $P_{lv1-load}$ and $P_{lv2-load}$ are the loading on LVAC-1 and LVAC-2 buses, respectively. P^*_{bess} is the BESS charging power reference.

B. MODE-2: PEAK LOAD SHAVING OPERATION

The mode-2 power flow diagram is shown in Fig. 2(b). The peak load shaving is typically employed to eliminate demand spikes in the system that causes the extreme power demands from the energy sources. This mode operates to support the grid during peak loading hours. The LVAC-1 load is supported either from the BESS or from the grid-2 through MVDC link. This mode is activated when the LVAC-1 load exceeds the predefined peak demand limit ($P_{peak-lim}$). The ST-1 MV converter active power reference is given by,

$$P^*_{mv1} = P_{peak-lim}, \quad \text{if } P_{lv1-load} > P_{peak-lim}. \tag{2}$$

P^*_{mv2} remains same as given in (1). If the BESS is available for discharge, the power is delivered from BESS. In the event of BESS unavailability, the power is transferred from grid-2 through MVDC line. Therefore, the BESS discharge power reference (P^*_{bess}) and the dc transfer power reference (P^*_t) are given by,

$$\begin{aligned} P^*_{bess} &= P^*_t \\ &= P_{peak-lim} - P_{lv1-load}, \quad \text{if } P_{lv1-load} > P_{peak-lim}. \end{aligned} \tag{3}$$

This active power support helps in reducing peak load demand on the MVAC-1 bus.

C. MODE-3: REVERSE POWER FLOW CONTROL

Reverse power flow occurs when the total generation from the PV source is higher than the total load. In that case, the balance power is supplied to grid. The mode-3 power flow diagram is shown in Fig. 2(c). The increased power production from PV sources at low-load periods causes reverse power flow in the MVAC grid that can cause voltage rise. This mode controls the reverse power flow in the MVAC side of the

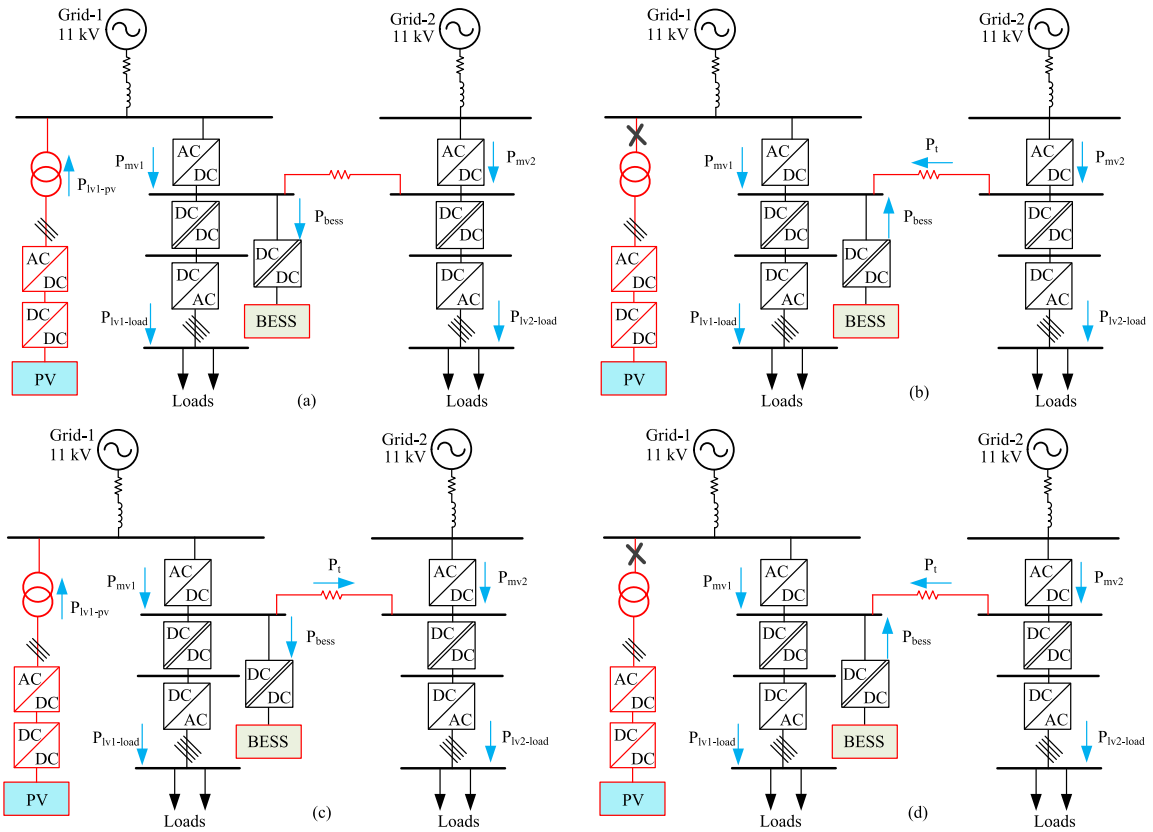

FIGURE 2. Power flow diagram of the system during various operating modes. (a) Mode-1. (b) Mode-2. (c) Mode-3. (d) Mode-4.

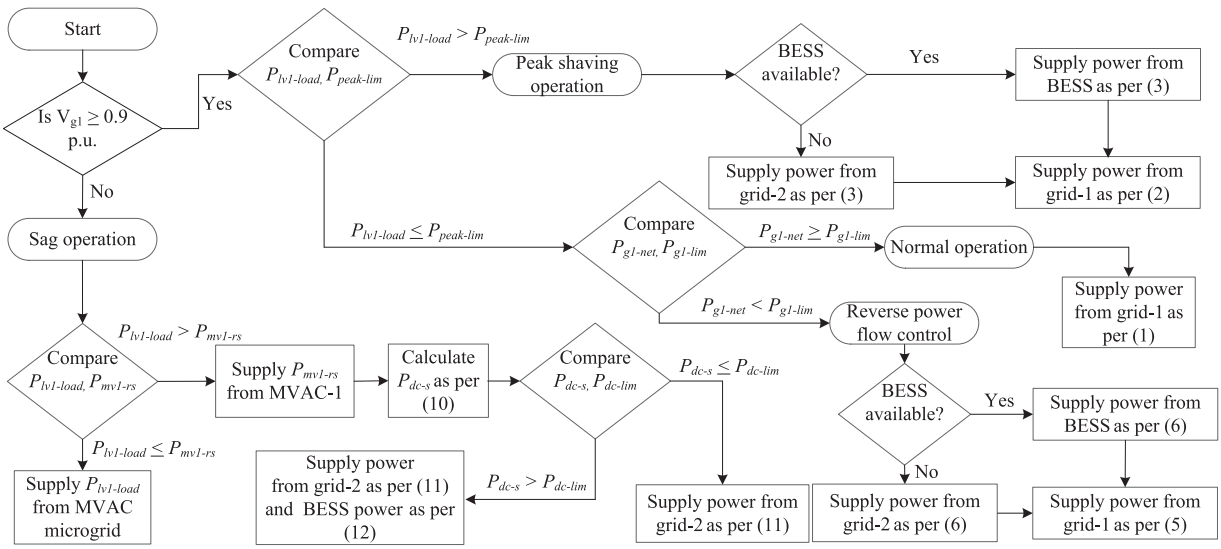

FIGURE 3. Flow-chart representation of modes of operation.

grid-1. The net power import (P_{g1-net}) in the grid-1 is given by,

$$P_{g1-net} = P_{lv1-load} - P_{lv1-pv} \tag{4}$$

where P_{lv1-pv} is the active power generation from PV generator. During low-load, peak-generation hours, the active power from PV is absorbed through ST-1 MV converter depending upon the predefined power export limit (P_{g1-lim}). The ST-1 MV converter reference power is given by,

$$P^*_{mv1} = P_{lv1-pv} - P_{g1-lim}, \quad \text{if } P_{g1-net} < P_{g1-lim}. \tag{5}$$

The ST-2 MV converter active power reference remain same as given in (1). The absorbed power is either used for BESS charging or if BESS is not available for charging,

the power is transferred to the grid-2. Therefore, the BESS charging power reference and the dc transfer power reference is given by,

$$P^*_{bess} = P^*_t = -P_{g1-net} - P_{g1-lim}, \quad \text{if } P_{g1-net} < P_{g1-lim}. \tag{6}$$

The extra absorption of active power limits the reverse power flow in grid-1 and the voltage rise conditions are avoided.

D. MODE 4: SAG OPERATION

The mode-4 power flow diagram is shown in Fig. 2(d). Voltage sags are caused by different faults in the grid and it affects the availability of power supply to the customers. If the MVAC-1 voltage magnitude is lower than 90% of the nominal value, the ST-1 operates in sag operating mode. For the detection of sag, the measured rms MVAC voltage is compared with a threshold magnitude of 0.9 p.u. [36]. If the magnitude falls below threshold value, the ST operation mode is changed to the voltage sag mode. In this mode, the ST-1 MV converter is controlled to continue the operation with reduced power absorption. Due to the constant power operation of grid-connected ST-1 MV converter, the absorption of currents increases during voltage sag to maintain the load power supply. In this paper, the ST-1 MV converter is controlled in coordination with ST-2 and BESS for ensuring the reliability of power supply for the LVAC-1 loads during grid-1 voltage sags.

The reactive power exchange is not considered during this operating mode and the apparent power rating (S_{mv1-rn}) of ST-1 MV converter during nominal microgrid voltage condition is equal to the active power rating (P_{mv1-rn}) given by,

$$P_{mv1-rn} = \sqrt{3} V_{g1-n} I_{mv1-r} \tag{7}$$

where V_{g1-n} is the MVAC-1 nominal rms voltage (L-L) and I_{mv1-r} is the ST-1 MV converter rms current rating. In the event of grid-1 MVAC voltage sag, the voltage (V_{g1-s}) is lower than the nominal value. For limiting the currents within the rating, the maximum apparent power (S_{mv1-rs}) that can be absorbed during sag is limited to a lower value as compared to S_{mv1-rn}. During sag, the active power rating (P_{mv1-rs}) which is same as the S_{mv1-rs} given by,

$$P_{mv1-rs} = \sqrt{3} V_{g1-s} I_{mv1-r} = M_s P_{mv1-rn}$$
$$\text{where } M_s = \frac{V_{g1-s}}{V_{g1-n}}. \tag{8}$$

In the case when ST-1 MV converter's effective rating during sag is less than the LVAC-1 demand, the balance power is transferred from grid-2 through MVDC line. However, the maximum power transfer during this mode is limited to a value (P_{dc-lim}) and the remaining power is absorbed from BESS.

The ST-1 MV converter power reference during voltage sag is given as,

$$P^*_{mv1} = \begin{cases} P_{lv1-load}, & \text{if } P_{lv1-load} \le P_{mv1-rs} \\ P_{mv1-rs}, & \text{otherwise.} \end{cases} \tag{9}$$

The MVDC power transfer is given by,

$$P_{dc-s} = \begin{cases} 0, & \text{if } P_{lv1-load} \le P_{mv1-rs} \\ P_{lv1-load} - P_{mv1-rs}, & \text{otherwise.} \end{cases} \tag{10}$$

The MVDC power transfer reference (P^*_t) is given by,

$$P^*_t = \begin{cases} -P_{dc-s}, & \text{if } P_{dc-s} \le P_{dc-lim} \\ -P_{dc-lim}, & \text{otherwise.} \end{cases} \tag{11}$$

The P^*_t is limited to a maximum value of P_{dc-lim} and BESS is activated if P_{dc-s} exceeds the P_{dc-lim}. The BESS power reference (P^*_{bess}) during the sag operation is given by,

$$P^*_{bess} = \begin{cases} 0, & \text{if } P_{dc-s} \le P_{dc-lim} \\ -(P_{dc-s} - P_{dc-lim}), & \text{otherwise.} \end{cases} \tag{12}$$

BESS transfers the remaining power to support the LVAC-1 load based on the requirement. The ST-2 MV converter reference remain same as given in (1).

IV. CONTROL OF ST AND BESS

In this paper, the ST-2 MV converter controls the MVDC link voltage, and ST-1 MV converter controls the power flow based on the requirement. This control concept can be extended to a three-grid/multi-grid system with one of the ST controlling the MVDC link voltage and other STs controlling the power flow based on the mode of operation. The storage can be integrated to the power flow controlling STs MVDC links and they can be controlled as per the control requirement. In this section, the control of ST MV, ST dc-dc, ST LV converters are explained. In addition, the BESS converter control is also explained. Overall control diagram is shown in Fig. 4.

A. ST-1 MV CONVERTER

The control block diagram is given in Fig. 5(a) and (b). The power reference generation according to operating modes is given in Fig. 5(a) and reference current generation is shown in Fig. 5(b). The aim of ST-1 MV converter is to support LVAC-1 loads and exchange power with ST-2 through MVDC link. It is also used to charge/discharge BESS. For the mode-1 to mode-4, the active power references are given by, (1), (2), (5), and (9), respectively. A generalized expression for the ST-1 MV converter reference power is given by

$$P^*_{mv1} = P_{lv1-load} + P^*_t + P^*_{bess}. \tag{13}$$

In mode-2 to mode-4, the inter-grid power transfer is controlled by ST-1 using indirect MVDC voltage control. Considering a constant dc link voltage at the MVDC-2 link, the

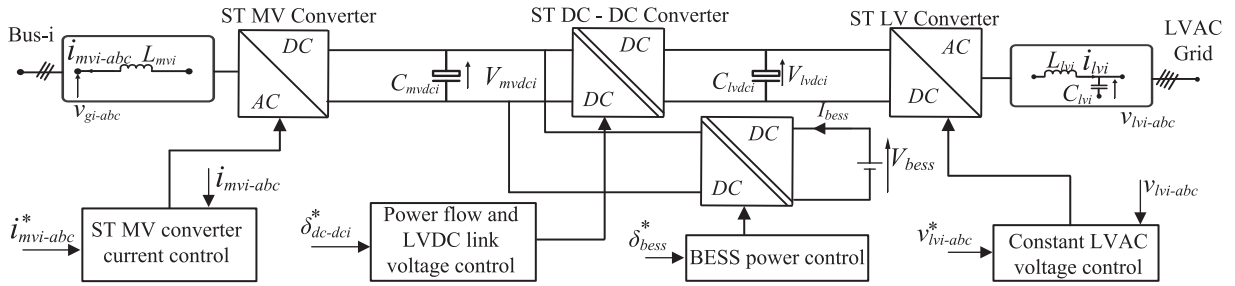

FIGURE 4. **Control of ST and BESS.**

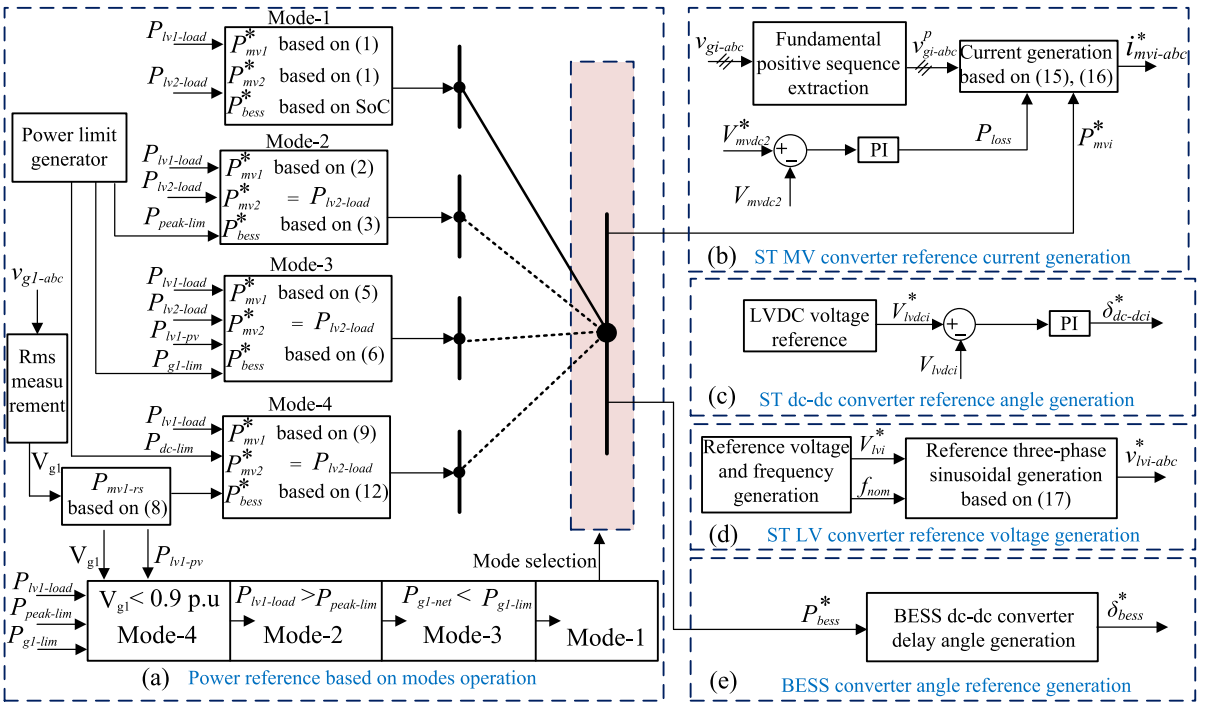

FIGURE 5. **Proposed control block diagram. (a) Power reference based on modes of operation. (b) ST MV converter reference current generation. (c) Reference phase angle generation of ST dc-dc converter. (d) Reference voltage generation of ST LV converter. (e) Reference phase angle generation of BESS converter.**

MVDC-1 voltage is expressed as

$$V_{mvdc1} = V_{mvdc2} + P_t^* \frac{2R_{dc}}{V_{mvdc2}} \tag{14}$$

where V_{mvdc1} and V_{mvdc2} are the voltages at MVDC-1 and MVDC-2 links, respectively. R_{dc} is the resistance of dc line. A positive P_t^* indicates that the power is transferred from grid-1 to grid-2, and a negative P_t^* indicates the power transfer from grid-2 to grid-1. The MVDC-1 voltage variation based on P_t^* is shown in Fig. 6. The P_t^{max} is the maximum power transfer and V_{mvdc1}^h, V_{mvdc1}^l are the maximum and minimum MVDC-1 voltages, respectively depending upon the direction of power transfer. At any operating power transfer P_{t-op}^*, the MVDC-1 voltage is V_{mvdc1}^o as shown in Fig. 6. The ST-1 MV power reference P_{mv1}^* is used with instantaneous symmetrical component theory (ISCT) [37] to generate the corresponding

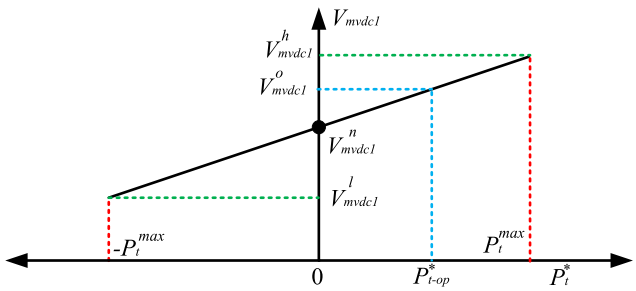

FIGURE 6. **MVDC-1 voltage variation with active power transfer.**

current references ($i_{mv1-abc}^*$) as given by

$$i_{mv1-a}^* = \frac{v_{g1a}^p + k_{pf1}(v_{g1b}^p - v_{g1c}^p)}{(v_{g1a}^p)^2 + (v_{g1b}^p)^2 + (v_{g1c}^p)^2}(P_{mv1}^*)$$

$$i^*_{mv1-b} = \frac{v^p_{g1b} + k_{pf1}(v^p_{g1c} - v^p_{g1a})}{(v^p_{g1a})^2 + (v^p_{g1b})^2 + (v^p_{g1c})^2}(P^*_{mv1})$$
$$i^*_{mv1-c} = \frac{v^p_{g1c} + k_{pf1}(v^p_{g1a} - v^p_{g1b})}{(v^p_{g1a})^2 + (v^p_{g1b})^2 + (v^p_{g1c})^2}(P^*_{mv1}) \quad (15)$$

where v^p_{g1a}, v^p_{g1b} and v^p_{g1c}, respectively are fundamental positive sequence MVAC-1 voltages of respective phases. k_{pf1} is the power factor control constant, and in this paper reactive power exchange is not considered, and therefore k_{pf1} is zero. These reference currents are maintained using PWM controller to generate switching pulses. Hysteresis based controller is used for controlling the ST MV converters due to its advantages such as simplicity in implementation, lesser computational requirement in the digital controller, low tracking errors, very good dynamic response, etc. [38].

B. ST-2 MV CONVERTER

The block-diagram representation of the power reference generation and reference current generation strategy is shown in Fig. 5(a) and (b), respectively. The ST-2 MV converter supplies the active power requirement at LVAC-2 bus. It also exchanges active power with grid-2 through MVDC distribution line. ST-2 MV converter maintains the dc link voltage at nominal value, and depending upon the MVDC-1 voltage magnitude, the power is exchanged with the ST-1. The reference (V^*_{mvdc2}) and measured (V_{mvdc2}) MVDC-2 voltages are compared and the error is passed through a proportional integral (PI) controller to generate the reference P_{loss}. The gains of PI controller are selected based on the symmetrical optimum method [39]. This power reference along with ST-2 MV active power reference generated in (1) are used in ISCT to generate current references ($i^*_{mv2-abc}$) as given by

$$i^*_{mv2-a} = \frac{v^p_{g2a} + k_{pf2}(v^p_{g2b} - v^p_{g2c})}{(v^p_{g2a})^2 + (v^p_{g2b})^2 + (v^p_{g2c})^2}(P^*_{mv2} + P_{loss})$$
$$i^*_{mv2-b} = \frac{v^p_{g2b} + k_{pf2}(v^p_{g2c} - v^p_{g2a})}{(v^p_{g2a})^2 + (v^p_{g2b})^2 + (v^p_{g2c})^2}(P^*_{mv2} + P_{loss}) \quad (16)$$
$$i^*_{mv2-c} = \frac{v^p_{g2c} + k_{pf2}(v^p_{g2a} - v^p_{g2b})}{(v^p_{g2a})^2 + (v^p_{g2b})^2 + (v^p_{g2c})^2}(P^*_{mv2} + P_{loss})$$

where v^p_{g2a}, v^p_{g2b} and v^p_{g2c}, respectively are fundamental positive sequence MVAC-2 voltages of respective phases. The power factor control constant $k_{pf2} = 0$, since there is no reactive power transfer. These reference currents are used with PWM controller to generate converter switching pulses.

C. ST DC-DC CONVERTER

The control block diagram is given in Fig. 5(c). For both ST-1 and ST-2, dc-dc converters are operated to transfer required power between MVDC and LVDC links. The symbol 'i' indicates terms related to i^{th} ST (i =1, 2). The voltage is maintained at a constant reference value for LVDC-1 and LVDC-2 links by the respective dc-dc converters. A PI controller generates a phase angle reference (δ^*_{dc-dci}) from the error generated by the comparison of reference LVDC-i voltage (V^*_{lvdci}) and corresponding measured value (V_{lvdci}). The PI controller gains are selected using symmetrical optimum method to obtain the appropriate phase angle output. Maintaining this phase angle difference between MVDC and LVDC side converter switches ensure the power flow and voltage control [35].

TABLE 2 Simulation Parameters

System quantities	Values
ST MV converters	L_{mvi} = 100 mH
ST LV converters	L_{lvi} = 0.5 mH, C_{lvi} = 20 μF
DC link capacitors	C_{mvdci} = 2000 μF, C_{lvdci} = 2500 μF
ST dc-dc converters	L_{mvdc} = 10 mH, f_{sw} = 1 kHz
BESS dc-dc converter	L_b = 10 mH, f_{sw} = 1 kHz

D. ST LV CONVERTER

A block-diagram is given in Fig. 5(d). The ST-1 and ST-2 LV converters are controlled similar to a grid forming voltage converter [2]. The reference rms LV voltage (V^*_{lvi}) at nominal frequency (f_{nom}) is used to generate the three-phase sinusoidal ($v^*_{lvi-abc}$) voltage as given by,

$$v^*_{lvi-a} = V^*_{lvi}\sqrt{2}\sin(\omega_{nom}t)$$
$$v^*_{lvi-b} = V^*_{lvi}\sqrt{2}\sin(\omega_{nom}t - 2\pi/3).$$
$$v^*_{lvi-c} = V^*_{lvi}\sqrt{2}\sin(\omega_{nom}t + 2\pi/3) \quad (17)$$

The reference three-phase voltages are maintained at the respective LVAC buses by the PWM controller.

E. BESS DC-DC CONVERTER

The power references are generated according to the mode of operation as shown in Fig. 5(a). During mode-1, the BESS charges from grid-1 to maintain the necessary SoC. During peak load shaving operation, based on the availability of energy, the grid-1 is supported from BESS. During reverse power flow control mode, as per requirement and availability, power is transferred from grid-1. In sag operation, the BESS supports the LVAC-1 load as per the algorithm shown in Fig. 3. Based on the charging/discharging power reference (P^*_{bess}) given in (3), (6) and (12), the controller generates the reference angle (δ^*_{bess}) as shown in Fig. 5(e). This angle is maintained between MVDC-1 and BESS side converter switches which ensures the required power exchange between BESS and MVDC-1 bus [34].

V. SIMULATION RESULTS

Simulation is conducted in PSCAD software and the parameters are shown in Table 1 and Table 2. Three cases are simulated in this paper.

Fig. 7 shows the operation with BESS support during peak loading on the grid-1. Till t = 10 s, the ST-1 and ST-2 MV converters supply their own LVAC loads. At t = 10 s, the loading on LVAC-1 bus is increased beyond the $P_{peak-lim}$.

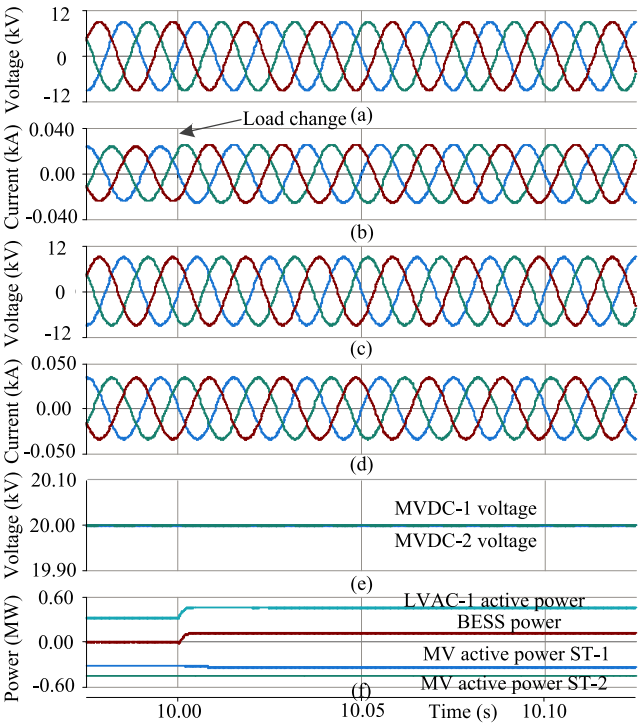

FIGURE 7. Simulation results for peak load shaving operation. (a) MVAC-1 voltages. (b) ST-1 MV converter currents. (c) MVAC-2 voltages. (d) ST-2 MV converter currents. (e) Dc link voltages. (f) Different active powers.

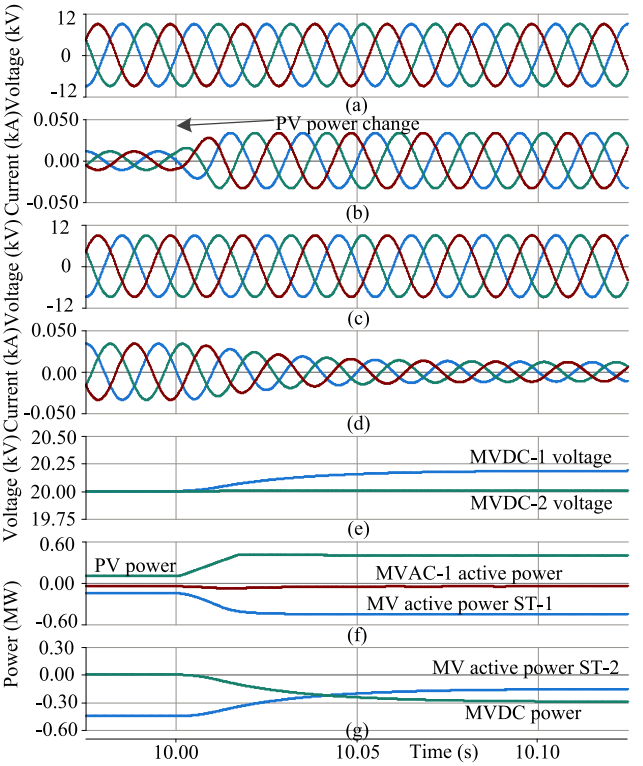

FIGURE 8. Simulation results during reverse power flow control. (a) MVAC-1 voltages. (b) ST-1 MV converter currents. (c) MVAC-2 voltages. (d) ST-2 MV converter currents. (e) Dc link voltages. (f) PV, ST-1 MV and MVAC-1 active powers. (g) ST-2 and MVDC active powers.

The BESS is available for discharge and supports the LVAC-1 loads and Fig. 7(a) and (c) show the MVAC-1 and MVAC-2 voltages, respectively. Fig. 7(b) and Fig. 7(d) show the ST-1 MV and ST-2 MV converter currents. The MVDC-1 and MVDC-2 voltages are shown in Fig. 7(e). In Fig. 7(f), different active powers are shown.

In the second case shown in Fig. 8, the reverse power flow control operation is exhibited. At $t = 10$ s, the PV output power increases and LVAC-1 loading is low during this time. The ST-1 absorbs the active power from grid-1 and since BESS is not available in this condition, power is transferred to the grid-2 through MVDC line. Fig. 8(a) and (c) show the MVAC-1 and MVAC-2 voltages, respectively. The ST MV converter currents are shown in Fig. 8(b) and (d) for ST-1 and ST-2, respectively. The ST-1 MV converter currents increase due to extra power absorption. Fig. 8(e) shows MVDC link voltages of ST-1 and ST-2 and MVDC-1 voltage increases above nominal value to control the power transfer. Fig. 8(f) shows PV, ST-1 MV and MVAC-1 active powers. The MVAC-1 active power remains nearly constant due to the increased absorption by ST-1 MV converter thereby avoiding reverse power flow. Fig. 8(g) shows the ST-2 and MVDC active powers.

In the third case shown in Fig. 9, the voltage sag operation is analyzed. Fig. 9(a) and (c) show the MVAC-1 and MVAC-2 voltages, respectively and MVAC-1 voltage decreases after experiencing a 40% sag. The ST MV converter currents are shown in Fig. 9(b) and (d) for ST-1 and ST-2. The ST-1 MV

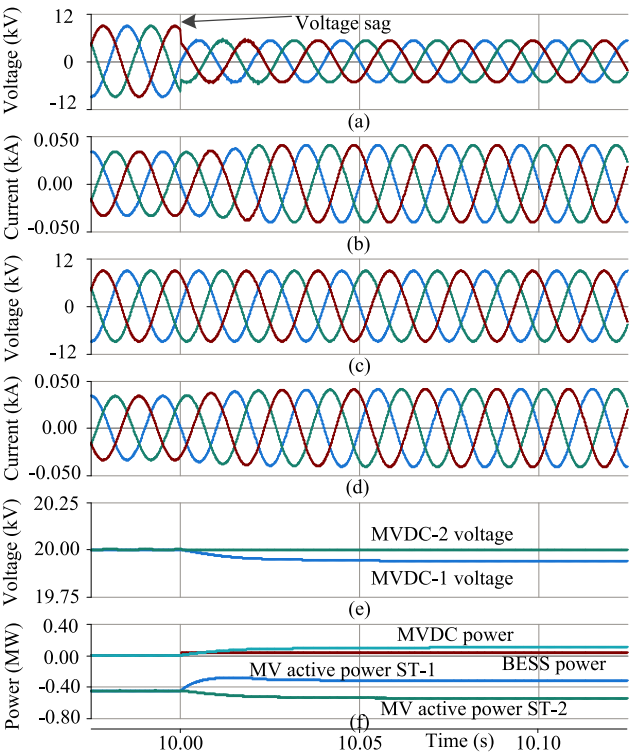

FIGURE 9. Simulation results during MVAC-1 voltage sag. (a) MVAC-1 voltages. (b) ST-1 MV converter currents. (c) MVAC-2 voltages. (d) ST-2 MV converter currents. (e) Dc link voltages. (f) Different active powers.

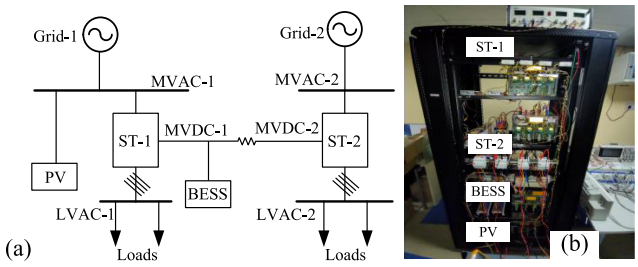

FIGURE 10. Laboratory prototype. (a) Schematic diagram. (b) Photograph.

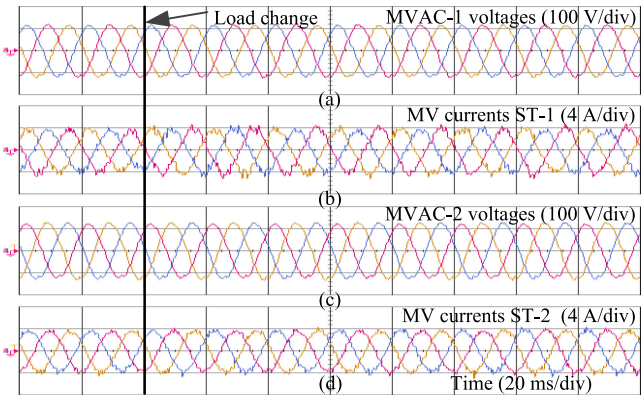

FIGURE 11. Experimental results during peak load shaving operation. (a) MVAC-1 voltages. (b) ST-1 MV converter currents. (c) MVAC-2 voltages. (d) ST-2 MV converter currents.

converter currents increase to the maximum rating. Fig. 9(e) shows MVDC bus voltages of ST-1 and ST-2. The MVDC-1 voltage decreases to transfer the demanded power from grid-2. Fig. 9(f) shows different active powers. The ST-1 and ST-2 MV converter active powers are shown. The active power is transferred from the grid-2 and since it reaches the maximum transferable power, BESS is also activated to supply the remaining power as per the flow-chart shown in Fig. 3.

VI. EXPERIMENTAL ANALYSIS

In the experiments, MVAC voltage is 150 V (L-L), and LVAC voltage is 110 V (L-L). Fig. 10(a) and (b), respectively show the schematic diagram and photograph of the experimental prototype. The experiment analysis shows all the cases described in simulation analysis.

In the first case, the peak load operation is analyzed. Fig. 11 and 12 show the results for the peak load operation. The ST-1 and ST-2 operate supplying the LVAC loads. The LVAC-1 load increased beyond the predefined peak load limit, and BESS supports the ST-1 loads. Fig. 11(a) and (c) show the three-phase voltages of MVAC-1 and MVAC-2, respectively. Fig. 11(b) and (d) show the MV currents for ST-1 and ST-2. The load change is marked in the Fig. 11 and 12. The dc link voltages are shown in Fig. 12(a). Different powers are shown in Fig. 12(b). This shows that the BESS power support lowers the peak demand on grid-1 and smooths the load curve.

In the second case, PV injection increase scenario is considered to show the reverse power flow case. Fig. 13 and 14 show

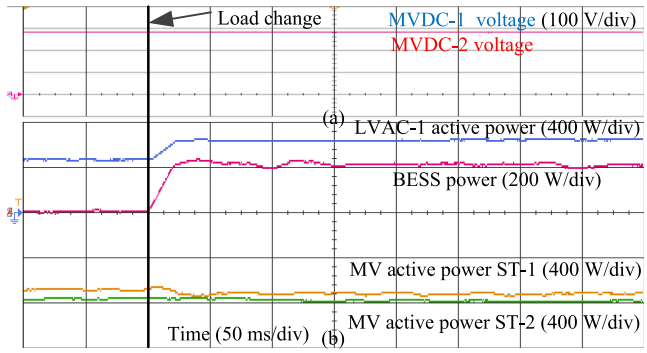

FIGURE 12. Experimental results during peak load shaving operation. (a) DC link voltages. (b) Different active powers.

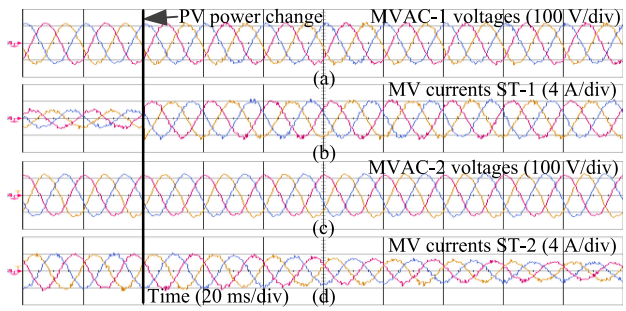

FIGURE 13. Experimental results during reverse power flow control. (a) MVAC-1 voltages. (b) ST-1 MV converter currents. (c) MVAC-2 voltages. (d) ST-2 MV converter currents.

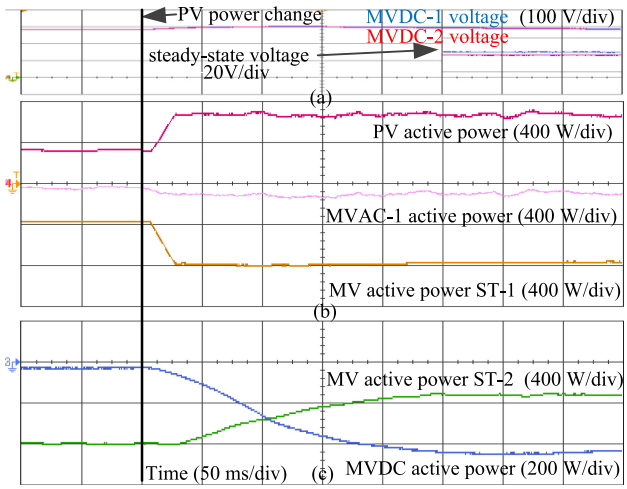

FIGURE 14. Experimental results during reverse power flow control. (a) Dc link voltages. (b) PV, ST-1 MV and MVAC-1 active powers. (c) ST-2 and MVDC active powers.

different waveforms. Fig. 13(a) and (c) show MVAC voltages for ST-1 and ST-2, respectively. ST-1 MV currents increase after the absorption of extra active power from PV source, and it is shown in Fig. 13(b). ST-2 MV currents decrease due to extra active power support from MVDC line as shown in Fig. 13(d). Dc link voltages are shown in Fig. 14(a). MVDC-1 link voltage increases to facilitate the active power transfer. Fig. 14(b) shows PV, ST-1 MV and MVAC-1 active powers.

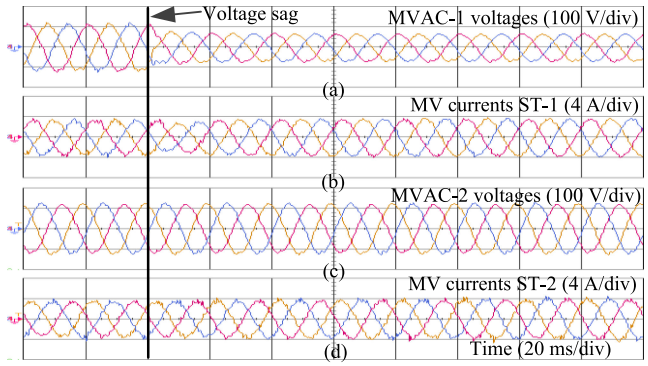

FIGURE 15. **Experimental results during MVAC-1 voltage sag. (a) MVAC-1 voltages. (b) ST-1 MV converter currents. (c) MVAC-2 voltages. (d) ST-2 MV converter currents.**

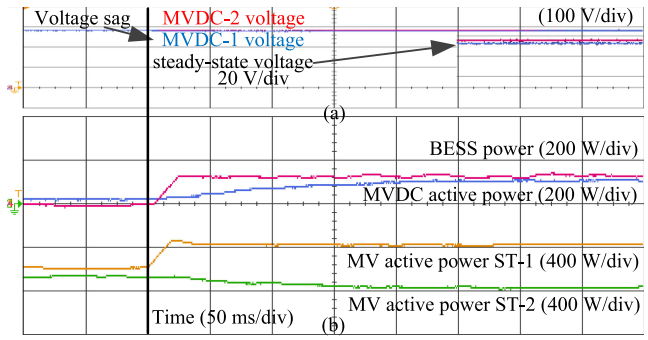

FIGURE 16. **Experimental results during MVAC-1 voltage sag. (a) Dc link voltages. (b) Different active powers.**

The MVAC-1 active power remains nearly constant even after the PV power increase. Fig. 14(c) shows the ST-2 MV and MVDC active powers. The reverse power control capability shows the ability of the system to reduce the voltage rise conditions.

In the third case, the MVAC-1 bus experiences a voltage sag and ST-1 active power is supported by the ST-2 and BESS. Fig. 15(a) shows the MVAC-1 voltages and the voltage sag is visible in the waveform. Fig. 15(b) shows the MV currents. Fig. 15(c) shows the MVAC-2 voltages and Fig. 15(d) shows ST-2 MV currents. Dc link voltages are shown in Fig. 16(a) and the MVDC-1 voltage decreases to import active power through MVDC line. Different powers are shown in Fig. 16(b). The uninterrupted operation during voltage sag improves the overall reliability of the system.

VII. CONCLUSION

This paper proposes operation of an MVDC interconnected meshed hybrid microgrid configuration enabled by ST and BESS during adverse grid conditions. The following advantages are achieved: (1) lower peak power demand from MVAC grid smooths the load curve and reduces the unmanageable high-load conditions on the grid, (2) reverse power flow control reduces the voltage rise conditions without the PV active power curtailment, and this helps in maximizing the energy extraction from PV sources, and (3) continuous operation of loads during grid voltage sags are helpful in reducing power interruption-hours in the system and this improves the reliability of power supply to the customer. The simulation and experimental results verify the findings.

REFERENCES

[1] X. Liang, "Emerging power quality challenges due to integration of renewable energy sources," *IEEE Trans. Ind. Appl.*, vol. 53, no. 2, pp. 855–866, Mar. 2017.

[2] J. Rocabert, A. Luna, F. Blaabjerg, and P. Rodriguez, "Control of power converters in ac microgrids," *IEEE Trans. Power Electron.*, vol. 27, no. 11, pp. 4734–4749, Nov. 2012.

[3] C. L. Masters, "Voltage rise: The big issue when connecting embedded generation to long 11 kv overhead lines," *Power Eng. J.*, vol. 16, no. 1, pp. 5–12, Feb. 2002.

[4] K. Mahmud, M. J. Hossain, and G. E. Town, "Peak-load reduction by coordinated response of photovoltaics, battery storage, and electric vehicles," *IEEE Access*, vol. 6, pp. 29353–29365, 2018.

[5] R. Kabiri, D. G. Holmes, B. P. McGrath, and L. G. Meegahapola, "LV grid voltage regulation using transformer electronic tap changing, with PV inverter reactive power injection," *IEEE J. Emerg. Sel. Top. Power Electron.*, vol. 3, no. 4, pp. 1182–1192, Dec. 2015.

[6] R. Tonkoski, L. A. C. Lopes, and T. H. M. El-Fouly, "Coordinated active power curtailment of grid connected PV inverters for overvoltage prevention," *IEEE Trans. Sustain. Energy*, vol. 2, no. 2, pp. 139–147, Apr. 2011.

[7] C. Kumar and M. K. Mishra, "Operation and control of an improved performance interactive dstatcom," *IEEE Trans. Ind. Electron.*, vol. 62, no. 10, pp. 6024–6034, Oct. 2015.

[8] *MVDC PLUS - the Grid Connector*. [Online]. Available: https://new.siemens.com/global/en/products/energy/medium-voltage/solutions/mvdc.html

[9] J. K. Steinke, P. Maibach, G. Ortiz, F. Canales, and P. Steimer, "Mvdc applications and technology," in *Proc. PCIM Europe; Int. Exhib. Conf. Power Electron., Intell. Motion*, Renewable Energy Energy Manage., May 2019, pp. 1–8.

[10] B. Silva, C. L. Moreira, L. Seca, Y. Phulpin, and J. A. Pecas Lopes, "Provision of inertial and primary frequency control services using offshore multiterminal hvdc networks," *IEEE Trans. Sustain. Energy*, vol. 3, no. 4, pp. 800–808, Oct. 2012.

[11] Y. Cao *et al.*, "A virtual synchronous generator control strategy for vsc-mtdc systems," *IEEE Trans. Energy Convers.*, vol. 33, no. 2, pp. 750–761, Jun. 2018.

[12] R. Bernacchi, "MVDC and Grid Interties: enabling new features in distribution, sub-transmission and industrial networks," [Online]. Available: https://library.e.abb.com/public/5fea768c835b4daeb8258bf950ddb05c/ABB%20MVDC_White%20paper.pdf?x-sign=X9LOXylnUBkKlMUPttFtrNFlHfODv7TYMZjoITkYE332BdplwYEgUSztjC9z/l58

[13] L. Zhang, J. Liang, W. Tang, G. Li, Y. Cai, and W. Sheng, "Converting ac distribution lines to DC to increase transfer capacities and DG penetration," *IEEE Trans. Smart Grid*, vol. 10, no. 2, pp. 1477–1487, Mar. 2019.

[14] L. F. Costa, G. D. Carne, G. Buticchi, and M. Liserre, "The smart transformer: A solid-state transformer tailored to provide ancillary services to the distribution grid," *IEEE Power Electron. Mag.*, vol. 4, no. 2, pp. 56–67, Jun. 2017.

[15] M. Liserre, G. Buticchi, M. Andresen, G. D. Carne, L. F. Costa, and Z. X. Zou, "The smart transformer: Impact on the electric grid and technology challenges," *IEEE Ind. Electron. Mag.*, vol. 10, no. 2, pp. 46–58, Jun. 2016.

[16] S. Bhattacharya, "Transforming the transformer," *IEEE Spectr.*, vol. 54, no. 7, pp. 38–43, Jul. 2017.

[17] F. Ruiz Allende, M. A. Perez, J. R. Espinosa, T. Gajowik, S. Stynski, and M. Malinowski, "Surveying solid-state transformer structures and controls: Providing highly efficient and controllable power flow in distribution grids," *IEEE Ind. Electron. Mag.*, vol. 14, no. 1, pp. 56–70, Mar. 2020.

[18] A. Q. Huang, Q. Zhu, L. Wang, and L. Zhang, "15 kv sic mosfet: An enabling technology for medium voltage solid state transformers," *CPSS Trans. Power Electron. Appl.*, vol. 2, no. 2, pp. 118–130, 2017.
[19] M. Liserre, M. Andresen, L. Costa, and G. Buticchi, "Power routing in modular smart transformers: Active thermal control through uneven loading of cells," *IEEE Ind. Electron. Mag.*, vol. 10, no. 3, pp. 43–53, Sep. 2016.
[20] V. Raveendran, M. Andresen, G. Buticchi, and M. Liserre, "Thermal stress based power routing of smart transformer with CHB and DAB converters," *IEEE Trans. Power Electron.*, vol. 35, no. 4, pp. 4205–4215, Apr. 2020.
[21] J. Falck, C. Felgemacher, A. Rojko, M. Liserre, and P. Zacharias, "Reliability of power electronic systems: An industry perspective," *IEEE Ind. Electron. Mag.*, vol. 12, no. 2, pp. 24–35, Jun. 2018.
[22] S. Peyghami, F. Blaabjerg, and P. Palensky, "Incorporating power electronic converters reliability into modern power system reliability analysis," *IEEE J. Emerg. Sel. Top. Power Electron.*, vol. 9, no. 2, pp. 1668–1681, Apr. 2021.
[23] D. Das, V. M. Hrishikesan, C. Kumar, and M. Liserre, "Smart transformer-enabled meshed hybrid distribution grid," *IEEE Trans. Ind. Electron.*, vol. 68, no. 1, pp. 282–292, Jan. 2021.
[24] H. V. M., A. K. Deka, and C. Kumar, "Capacity enhancement of a radial distribution grid using smart transformer," *IEEE Access*, vol. 8, pp. 72411–72423, 2020.
[25] C. Kumar, R. Zhu, G. Buticchi, and M. Liserre, "Sizing and SOC management of a smart-transformer-based energy storage system," *IEEE Trans. Ind. Electron.*, vol. 65, no. 8, pp. 6709–6718, Aug. 2018.
[26] V. M. Hrishikesan, C. Kumar, and M. Liserre, "Flexible power transfer in smart transformer interconnected microgrids," in *Proc. 44th Annu. Conf. IEEE Ind. Electron. Soc.*, Oct. 2018, pp. 5535–5540.
[27] V. M. Hrishikesan and C. Kumar, "Smart transformer based meshed hybrid microgrid with mvdc interconnection," in *Proc. IECON 46th Annu. Conf. IEEE Ind. Electron. Soc.*, 2020, pp. 4961–4966.
[28] G. De Carne, G. Buticchi, M. Liserre, and C. Vournas, "Real-time primary frequency regulation using load power control by smart transformers," *IEEE Trans. Smart Grid*, vol. 10, no. 5, pp. 5630–5639, Sep. 2019.
[29] D. Shah and M. L. Crow, "Online volt-var control for distribution systems with solid-state transformers," *IEEE Trans. Power Del.*, vol. 31, no. 1, pp. 343–350, Feb. 2016.
[30] H. V M, D. Das, C. Kumar, H. B. Gooi, M. Saad, and X. Guo, "Increasing voltage support using smart power converter based energy storage system and load control," *IEEE Trans. Ind. Electron.*, p. 1, 2020, doi: 10.1109/TIE.2020.3042165.
[31] S. Giacomuzzi, M. Langwasser, G. De Carne, G. Buja, and M. Liserre, "Smart transformer-based medium voltage grid support by means of active power control," *CES Trans. Elect. Machines Syst.*, vol. 4, no. 4, pp. 285–294, Dec. 2020.
[32] G. De Carne, G. Buticchi, Z. Zou, and M. Liserre, "Reverse power flow control in a st-fed distribution grid," *IEEE Trans. Smart Grid*, vol. 9, no. 4, pp. 3811–3819, Jul. 2018.
[33] S. Giacomuzzi, G. De Carne, S. Pugliese, G. Buja, M. Liserre, and A. Kazerooni, "Synchronization of low voltage grids fed by smart and conventional transformers," *IEEE Trans. Smart Grid*, p. 1, 2021, doi: 10.1109/TSG.2021.3054478.
[34] S. Inoue and H. Akagi, "A bidirectional DC-DC converter for an energy storage system with galvanic isolation," *IEEE Trans. Power Electron.*, vol. 22, no. 6, pp. 2299–2306, Nov. 2007.
[35] S. Falcones, R. Ayyanar, and X. Mao, "A DC DC multiport-converter-based solid-state transformer integrating distributed generation and storage," *IEEE Trans. Power Electron.*, vol. 28, no. 5, pp. 2192–2203, May 2013.
[36] A. Camacho, M. Castilla, J. Miret, L. G. de Vicuña, and R. Guzman, "Positive and negative sequence control strategies to maximize the voltage support in resistive-inductive grids during grid faults," *IEEE Trans. Power Electron.*, vol. 33, no. 6, pp. 5362–5373, Jun. 2018.
[37] A. Ghosh and G. Ledwich, *Power Quality Enhancement Using Custom Power Devices*. Springer Science & Business Media, 2012.
[38] M. P. Kazmierkowski and L. Malesani, "Current control techniques for three-phase voltage-source pwm converters: A survey," *IEEE Trans. Ind. Electron.*, vol. 45, no. 5, pp. 691–703, Oct. 1998.
[39] R. Teodorescu, M. Liserre, and P. Rodriguez, *Grid Converters for Photovoltaic and Wind Power Systems*. Hoboken, NJ, USA: John Wiley & Sons, vol. 29, 2011.

HRISHIKESAN V M (Student Member, IEEE) received the B.Tech. degree in electrical and electronics engineering from Government Engineering College, Thrissur, India, in 2011 and the M.Tech. degree in power systems from the National Institute of Technology, Trichy, India, in 2014. He is currently a Research Scholar with the Department of Electronics and Electrical Engineering, Indian Institute of Technology Guwahati, Guwahati, India. His research interests include applications of power electronics in power systems and power quality.

CHANDAN KUMAR (Senior Member, IEEE) received the B.Sc. degree from the Muzaffarpur Institute of Technology, Muzaffarpur, India, in 2009, the M.Tech. degree from the National Institute of Technology, Trichy, India, in 2011, and the Ph.D. degree from the Indian Institute of Technology Madras, Chennai, India, in 2014, all in electrical engineering.

Since 2015, he has been working as Assistant Professor in electronics and electrical engineering Department, Indian Institute of Technology Guwahati, India. In 2016–17, he worked as Alexander von Humboldt Research Fellow with Chair of Power Electronics, University of Kiel, Kiel, Germany. He is an Associate Editor of IEEE ACCESS, IEEE OPEN JOURNAL OF POWER ELECTRONICS, and IEEE OPEN JOURNAL OF THE INDUSTRIAL ELECTRONICS SOCIETY. His research interests include power electronics application in power system, power quality, and renewable energy.